Synthesis and optical properties of single-crystalline $SnS_{1-x}Se_x$ nanobelts

Shengru Wang, Xiaofang Lai, Bingsheng Du, Junhao Ma, Peihua Wang, and Jikang Jian [a)]
School of Physics and Optoelectronic Engineering, Guangdong University of Technology, Guangzhou 510006, China

(Received 27 June 2020; accepted 28 September 2020)

In this work, $SnS_{1-x}Se_x$ ternary nanobelts were synthesized by a facile hydrothermal method without the assistance of surfactants. The structure, morphology, microstructure, compositions, chemical valences, phonon modes, and optical band gaps of the $SnS_{1-x}Se_x$ nanobelts were characterized in detail. The results indicate that the $SnS_{1-x}Se_x$ nanobelts have uniform one-dimensional morphology and are single crystals with high crystallinity. Se is incorporated into the SnS lattice to substitute for S-forming ternary $SnS_{1-x}Se_x$ alloy. With the increase of Se doping concentration, the optical band gaps of the nanobelts gradually decrease from 1.15 to 1.01 eV, confirming the tunable optical property achieved here. © *The Author(s), 2020. Published by Cambridge University Press on behalf of International Centre for Diffraction Data.* [doi:10.1017/S0885715620000615]

Key words: $SnS_{1-x}Se_x$, nanobelts, single crystal, band gap

I. INTRODUCTION

One-dimensional (1D) nanomaterials such as nanobelts, nanowires, and nanotubes have attracted intensive attention due to the unique properties and great technological importance for past decades. IV-metal chalcogenides, including (Sn, Pb)(S, Se, Te), are narrow-gap semiconductors with promising applications in the fields of near-infrared photodetecting (Wang *et al.*, 2015; Zhou *et al.*, 2016; Yao *et al.*, 2017), thermoelectric (Biswas *et al.*, 2012; Zhao *et al.*, 2014; Li *et al.*, 2017b), and photovoltaic devices (Ramakrishna Reddy *et al.*, 2006; Zhao *et al.*, 2010; Zhang *et al.*, 2014). Among those compounds, SnS possesses layered orthorhombic structures with direct and indirect band gaps of about 1.2–1.7 eV and 1.0–1.1 eV, respectively (Lu *et al.*, 2019), suggesting its potential for photovoltaic cells because of the good match for the solar radiation spectrum (Vidal *et al.*, 2012). In addition, SnS has lower toxicity to the environment and is more abundant in earth as compared with other metal chalcogenides. Recently, Se-doped SnS single crystals have been reported to be a low-cost thermoelectric material with high-performance, inspiring wide interest quickly (He *et al.*, 2019). Numerous researches have indicated the improved or optimized properties achieved in the nanostructured materials compared with their bulk counterparts. To date, although some routes have been reported to obtain SnS and SnSe 1D nanostructures, such as liquid phase method (Chen *et al.*, 2000; Lu *et al.*, 2012; Guo *et al.*, 2017), chemical vapor deposition (CVD) (Yue *et al.*, 2011; Liu *et al.*, 2017), vacuum thermal evaporation (Butt *et al.*, 2012; Suryawanshi *et al.*, 2014), and electrodeposition (Biçer and Şişman, 2011; Steichen *et al.*, 2013), $SnS_{1-x}Se_x$ ternary nanobelts with high crystallinity and tunable physical properties have not been reported.

In this paper, the Se-doped SnS nanobelts were prepared by a facile hydrothermal method. The phases, morphology, microstructures, chemical compositions and valences, phonon modes, and optical property of the $SnS_{1-x}Se_x$ nanobelts were well characterized, indicating that well-crystallized Se-doped SnS single-crystalline nanobelts were successfully synthesized and the band gaps were tuned by Se doping.

II. EXPERIMENTAL

A. Synthesis of $SnS_{1-x}Se_x$ nanobelts

All chemicals were directly used here without further purification. $SnCl_2{\cdot}2H_2O$ (99.999%, Aladdin), $CO(NH_2)_2$ (urea, 99.999%, Aladdin), CH_3CSNH_2 (TAA, ≥ 99.0%, Aladdin), and Se (99.999%, Alfa Aesar) were used as raw materials. In this work, Se-doped SnS ($SnS_{1-x}Se_x$) nanobelts with nominal compositions of $x = 0$, 0.1, 0.2, 0.4, and 0.5 were prepared by a facile hydrothermal method (Lu *et al.*, 2012). In a typical run, a certain amount of Se was dispersed in 80 ml deionized water, stirred for about 10 min, and then 20 mmol urea, a certain amount of TTA, and 1.2 mmol $SnCl_2{\cdot}2H_2O$ were added in order. After stirring for 5 min, the obtained solution was transferred to an autoclave and kept at 170 °C for 10 h. After the reaction, the precipitates were collected, washed several times with deionized water and alcohol, and dried at 60 °C.

B. Characterizations

The phase, chemical compositions, morphology, and microstructures of the samples were characterized by X-ray diffraction (XRD; D/max-2550X), X-ray photoelectron spectroscopy (XPS; Thermo escalab 250Xi), field-emission scanning electron microscopy (SEM; Hitachi SU8220) with energy-dispersive X-ray spectroscopy (EDS), and transmission electron microscopy (TEM; FEI Talos F200). The

[a)]Author to whom correspondence should be addressed. Electronic mail: jianjikang@126.com

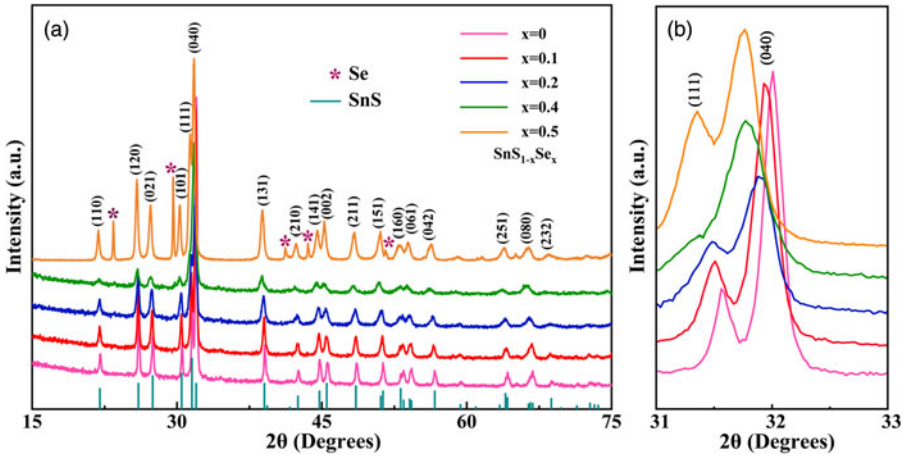

Figure 1. (a) XRD patterns of $SnS_{1-x}Se_x$ nanobelts (* labels the peaks of Se) with different nominal doping compositions x and (b) the enlarged XRD peaks of (040) and (111).

phonon modes and band gaps of the samples were examined by a micro confocal Raman spectrometer (HORIBA LabRAM HR Evolution) and an ultraviolet–visible–near-infrared spectrophotometer (UV–Vis–NIR; UV-3600 Plus), respectively.

III. RESULT AND DISCUSSION

Figure 1(a) shows the XRD patterns of $SnS_{1-x}Se_x$ nanobelts with different nominal doping compositions ($x = 0$, 0.1, 0.2, 0.4, and 0.5) synthesized here. The main diffraction peaks of all samples can be indexed to orthorhombic SnS (ICDD PDF No. 00-039-0354). The strongest diffraction peak is due to the reflection of (040) plane that has the largest spacing in orthorhombic SnS. No impurity phase can be detected in the samples with $x \leq 0.4$. The diffraction peaks of Se appear with $x = 0.5$, indicating that the nominal doping limitation of Se under the present synthetic conditions is below 0.5. It is worth noting that ICDD PDF No. 00-048-1225 reports a compound of $SnSe_{0.5}S_{0.5}$ that was prepared by a pyrolysis route using organometallic precursors of bis(triphenyl tin) sulfide and bis(triphenyl tin) selenide under He atmosphere. In our case, the $Sn(S_{1-x}Se_x)$ nanobelts were synthesized by a hydrothermal technique using Se powder as Se source. It was found that the impurity phase of Se appeared when the starting nominal concentration of Se is more than 0.5. In addition, the diffraction peaks all slightly shift to small angles with the increase of Se concentration [Figure 1(b)], suggesting that Se has been incorporated into the lattice as the substitution for S, which is consistent with the previous literature (Kafashan *et al.*, 2017; Khan *et al.*, 2018). Tables I–IV show the XRD data and the calculated lattice parameters for the $SnS_{1-x}Se_x$ nanobelts, clearly demonstrating the structural variation caused by Se doping. Noting that the x values for the samples in the tables were actual values determined by EDS, as discussed below.

The morphology and microstructure of $SnS_{1-x}Se_x$ nanobelts were characterized by SEM and TEM. As shown in Figure 2, all the samples are composed of a large number of nanobelts with uniform morphology. The elemental compositions of S and Se in the doped samples were obtained by EDS. The ratios of S:Se were 37.06(±0.15%):3.99(±0.08%), 40.17 (±0.25%):3.99(±0.14%), and 34.38 (±0.17%):10.06 (±0.17%) for the samples with nominal $x = 0.1$, 0.2, and 0.4, respectively, corresponding to the Se concentrations being $x = 0.097$, 0.13, and 0.23. Thereafter, x refers to the EDS value. The sizable changes between nominal and final concentrations in the samples imply that it is difficult to incorporate high-concentration Se into SnS nanobelts using Se powder as Se source through the present hydrothermal reaction. With the increase of Se concentration, the nanobelts have no

TABLE I. The XRD data of the SnS nanobelts. Fn is the Smith–Snyder figure of merit

(*hkl*)	$2\theta_{obs}$ (°)	$2\theta_{cal}$ (°)	$\Delta 2\theta$ (°)	d_{obs} (Å)	d_{cal} (Å)	$(I/I_0)_{obs}$
(110)	22.064	22.045	−0.019	4.0254	4.0287	7
(120)	26.037	26.046	0.009	3.4195	3.4183	20
(021)	27.48	27.487	0.007	3.243	3.2422	14
(101)	30.501	30.5	−0.001	2.9283	2.9285	13
(111)	31.553	31.553	0	2.8331	2.8331	29
(040)	31.996	31.994	−0.002	2.7949	2.795	100
(131)	39.084	39.072	−0.012	2.3028	2.3035	13
(210)	42.553	42.545	−0.008	2.1228	2.1231	5
(141)	44.76	44.76	0	2.0231	2.0231	9
(150)	45.598	45.614	0.016	1.9878	1.9872	8
(230)	48.616	48.625	0.009	1.8712	1.8709	8
(151)	51.324	51.33	0.006	1.7787	1.7785	8
(160)	53.451	53.464	0.013	1.7128	1.7124	5
(061)	54.288	54.267	−0.021	1.6884	1.689	6
(042)	56.68	56.671	−0.009	1.6226	1.6229	5
(251)	64.219	64.223	0.004	1.4492	1.4491	2
(171)	66.582	66.57	−0.012	1.4033	1.4036	4
(080)	66.817	66.822	0.005	1.399	1.3989	5
(242)	72.754	72.771	0.017	1.2987	1.2985	2
(113)	75.224	75.227	0.003	1.2621	1.2621	2
(341)	78.268	78.256	−0.012	1.2205	1.2206	2
Lattice constant (Å)	$a = 4.3304$ (7), $b = 11.1994$ (17), $c = 3.9886$ (6)					
Volume of cell (Å^3)	$V = 193.44$ (9)					
	$F_{21} = 32.7$ (0.0088, 73)					

https://doi.org/10.1017/S0885715620000615 Published online by Cambridge University Press

TABLE II. The XRD data of the $SnS_{0.903}Se_{0.097}$ nanobelts. Fn is the Smith–Snyder figure of merit

(*hkl*)	$2\theta_{obs}$ (°)	$2\theta_{cal}$ (°)	$\Delta 2\theta$ (°)	d_{obs} (Å)	d_{cal} (Å)	$(I/I_0)_{obs}$
(110)	21.992	22.019	0.027	4.0384	4.0335	3
(120)	26.034	26.019	−0.015	3.4198	3.4218	11
(021)	27.43	27.454	0.024	3.2489	3.246	8
(101)	30.476	30.47	−0.006	2.9307	2.9313	4
(111)	31.528	31.523	−0.005	2.8353	2.8357	16
(040)	31.971	31.963	−0.008	2.797	2.7977	100
(131)	39.037	39.041	0.004	2.3055	2.3052	8
(210)	42.524	42.523	−0.001	2.1241	2.1242	3
(141)	44.734	44.729	−0.005	2.0242	2.0244	6
(150)	45.573	45.584	0.011	1.9888	1.9884	5
(211)	48.516	48.516	0	1.8749	1.8749	4
(151)	51.321	51.298	−0.023	1.7788	1.7795	6
(160)	53.423	53.433	0.01	1.7137	1.7133	3
(061)	54.239	54.233	−0.006	1.6898	1.69	5
(042)	56.606	56.633	0.027	1.6246	1.6239	3
(251)	64.189	64.196	0.007	1.4498	1.4496	2
(080)	66.788	66.788	0	1.3995	1.3995	6
(113)	75.194	75.184	−0.01	1.2625	1.2627	2
Lattice constant (Å)	$a = 4.3296$ (15), $b = 11.2000$ (25), $c = 3.9893$ (8)					
Volume of cell (Å^3)	$V = 193.45$ (15)					
	$F_{18} = 23.5$ (0.0105, 73)					

TABLE IV. The XRD data of the $SnS_{0.77}Se_{0.23}$ nanobelts. Fn is the Smith–Snyder figure of merit

(*hkl*)	$2\theta_{obs}$ (°)	$2\theta_{cal}$ (°)	$\Delta 2\theta$ (°)	d_{obs} (Å)	d_{cal} (Å)	$(I/I_0)_{obs}$
(110)	21.814	21.816	0.002	4.0709	4.0706	2
(120)	25.802	25.792	−0.01	3.4501	3.4513	10
(021)	27.32	27.327	0.007	3.2617	3.2609	7
(101)	30.288	30.292	0.004	2.9485	2.9481	6
(040)	31.71	31.719	0.009	2.8195	2.8187	100
(131)	38.797	38.79	−0.007	2.3192	2.3196	11
(210)	42.137	42.137	0	2.1427	2.1427	4
(220)	44.469	44.477	0.008	2.0356	2.0353	7
(150)	45.231	45.224	−0.007	2.0031	2.0034	7
(230)	48.173	48.175	0.002	1.8874	1.8873	5
(112)	50.852	50.849	−0.003	1.7941	1.7942	7
(122)	52.874	52.889	0.015	1.7301	1.7297	4
(231)	53.663	53.658	−0.005	1.7065	1.7067	6
(132)	56.183	56.173	−0.01	1.6358	1.6361	4
(250)	58.834	58.835	0.001	1.5683	1.5682	2
(171)	66.058	66.044	−0.014	1.4132	1.4135	6
(181)	74.562	74.573	0.011	1.2717	1.2715	2
Lattice constant (Å)	$a = 4.3677$ (5), $b = 11.2746$ (9), $c = 3.9976$ (5)					
Volume of cell (Å^3)	$V = 196.86$ (6)					
	$F_{17} = 33.8$ (0.0068, 74)					

significant change in morphology. The lengths of the nanobelts are several micrometers to over 10 μm, the thickness is approximately 30 nm and the average width is about 225, 198, 191, and 178 nm for $x = 0$, 0.097, 0.13, and 0.23, respectively. TEM morphology images in Figures 2(b) and 2(g) for SnS and $SnS_{0.903}Se_{0.097}$ samples clearly show that the nanobelts have a smooth surface. HRTEM images of individual nanobelts in Figures 2(c) and 2(h) display the clear lattice fringes, and the crystal planes of (101) and (10-1) of orthorhombic SnS can be well-resolved, indicating that the top/bottom surfaces of the nanobelts are ±(010) planes. The result is consistent with the preferred orientation of (040) diffraction observed in the XRD patterns. The nanobelts have triangular tops [see Figures 2(e) and 2(j)] that are similar to the previous observation for SnSe nanobelts (Guo *et al.*, 2017). The HRTEM and the corresponding FFT images [Figures 2(d) and 2(i)] reveal that the nanobelts are single crystals with high crystallinity. The EDS elemental mapping for individual nanobelts [Figures 2(e) and 2(j)] illustrate S, Sn, and Se uniformly distribute in the nanobelts, revealing that Se was doped into the SnS nanobelt uniformly.

TABLE III. The XRD data of the $SnS_{0.87}Se_{0.13}$ nanobelts. Fn is the Smith–Snyder figure of merit

(*hkl*)	$2\theta_{obs}$ (°)	$2\theta_{cal}$ (°)	$\Delta 2\theta$ (°)	d_{obs} (Å)	d_{cal} (Å)	$(I/I_0)_{obs}$
(110)	21.967	21.975	0.008	4.0429	4.0415	13
(120)	25.957	25.966	0.009	3.4298	3.4286	33
(021)	27.35	27.355	0.005	3.2582	3.2576	23
(101)	30.396	30.381	−0.015	2.9382	2.9397	21
(111)	31.447	31.433	−0.014	2.8425	2.8437	52
(040)	31.89	31.888	−0.002	2.8039	2.8041	100
(131)	38.93	38.941	0.011	2.3115	2.3109	22
(210)	42.445	42.465	0.02	2.1279	2.1269	8
(141)	44.603	44.621	0.018	2.0298	2.0291	13
(002)	45.287	45.282	−0.005	2.0008	2.001	11
(211)	48.436	48.426	−0.01	1.8778	1.8782	13
(151)	51.192	51.18	−0.012	1.783	1.7834	12
(122)	52.954	52.938	−0.016	1.7277	1.7282	5
(160)	53.347	53.329	−0.018	1.7159	1.7164	9
(061)	54.079	54.102	0.023	1.6944	1.6937	9
(042)	56.443	56.447	0.004	1.6289	1.6288	8
(250)	59.228	59.249	0.021	1.5588	1.5583	3
(212)	63.829	63.812	−0.017	1.4571	1.4574	6
(171)	66.398	66.39	−0.008	1.4068	1.4069	8
(062)	68.655	68.65	−0.005	1.3659	1.366	3
(162)	72.495	72.492	−0.003	1.3027	1.3028	2
(113)	74.881	74.9	0.019	1.267	1.2668	3
Lattice constant (Å)	$a = 4.3311$ (8), $b = 11.2165$ (13), $c = 4.0020$ (5)					
Volume of cell (Å^3)	$V = 194.42$ (8)					
	$F_{22} = 25.1$ (0.0120, 73)					

The oxidation states of the elements in the SnS and $SnS_{0.903}Se_{0.097}$ nanobelts are characterized by XPS. Figure 3 shows the XPS peaks of S 2*p*, Sn 3*d*, and Se 3*d*, for the two samples, respectively. As shown in Figures 3(a) and 3(c), the peaks at 160.6 and 161.7 eV correspond to S $2p_{3/2}$ and S $2p_{1/2}$, confirming the S^{2-} oxidation state (Cheng and Conibeer, 2011). The Sn $3d_{3/2}$ peaks at 493.7 eV and the Sn $3d_{5/2}$ peaks at 485.3 eV correspond to Sn^{2+} oxidation states, and the Sn $3d_{3/2}$ peaks at 494.7 eV and the Sn $3d_{5/2}$ peaks at 486.3 eV correspond to Sn^{4+} oxidation states (Cheng and Conibeer, 2011; Baby and Mohan, 2019), respectively, which reveals the presence of SnS_2 or Sn_2S_3 phases in the nanobelts (Cheng and Conibeer, 2011). The separation of Sn $3d_{3/2}$ and Sn $3d_{5/2}$ is about 8.4 eV, which is consistent with the previous literature value (Li *et al.*, 2017a). The peaks at 53.1 and 53.9 eV correspond to Se $3d_{5/2}$ and Se $3d_{3/2}$, which is attributed to Se^{2-} (Franzman *et al.*, 2010). The

https://doi.org/10.1017/S0885715620000615 Published online by Cambridge University Press

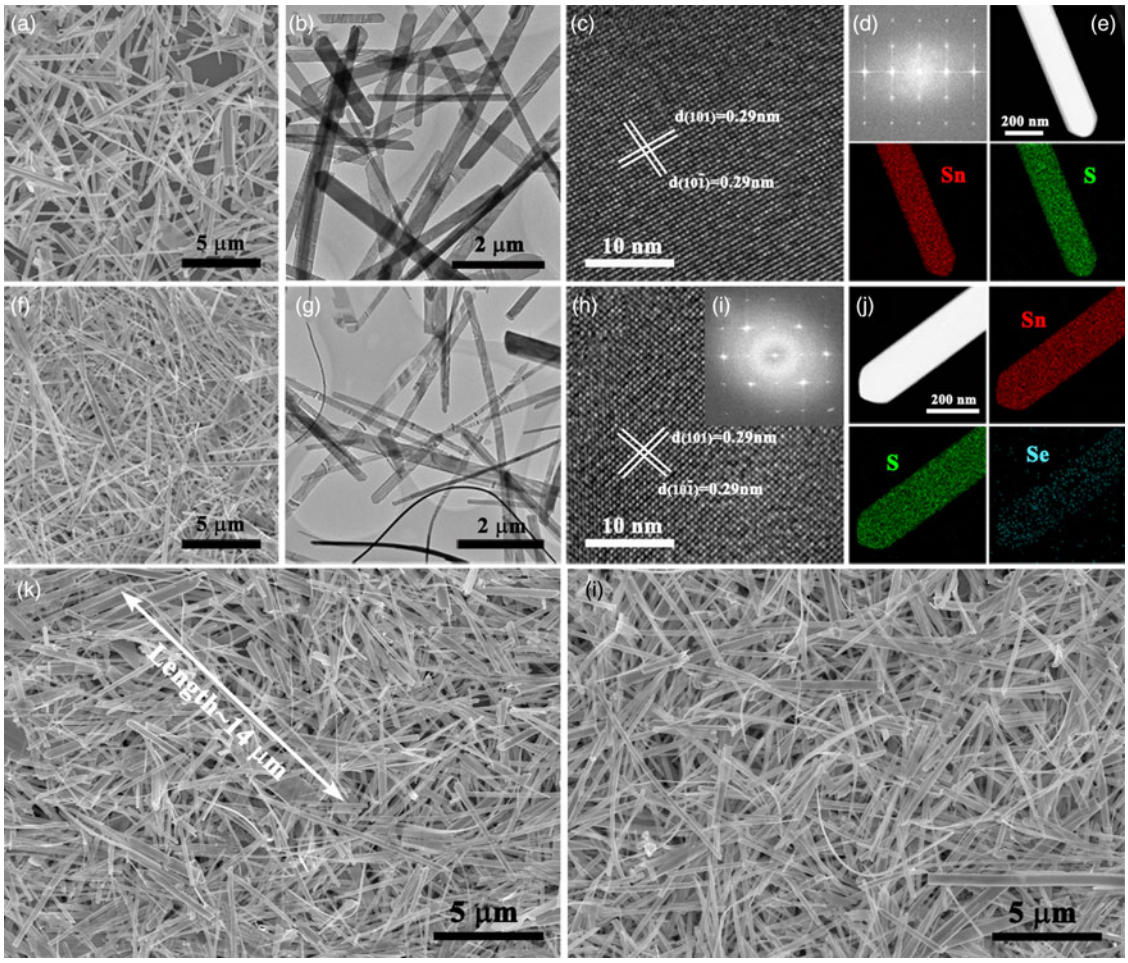

Figure 2. (a,f,k,l) SEM images of $SnS_{1-x}Se_x$ ($x = 0$, 0.097, 0.13, and 0.23, respectively). (b, and (g) TEM images, (c,h) HRTEM images, (d,i) SAED patterns obtained by fast Fourier transformation, and (e,j) EDS mapping correspond to SnS and $SnS_{0.903}Se_{0.097}$ nanobelts, respectively.

XPS results indicate the presence of (S^{2-}, Sn^{2+}, Sn^{4+}) and (S^{2-}, Sn^{2+}, Sn^{4+}, Se^{2-}) in SnS and Se-doped nanobelts, respectively. Given no the second phase detected by the XRD examination, SnS_2 or Sn_2S_3 should be trace amount of impurities in the samples.

Figure 4 shows the Raman spectra of the $SnS_{1-x}Se_x$ nanobelts. Based on the previous reports (Sohila *et al.*, 2011; Iqbal *et al.*, 2013; Cao *et al.*, 2019; Sarkar *et al.*, 2020), the main peaks at 92, 216, and 305 cm^{-1} are assigned to A_g mode and the peaks at 156 and 182 cm^{-1} are assigned to B_{3g} and B_{2g} mode of orthorhombic SnS, respectively. The mode at 305 cm^{-1} is probably due to Sn_2S_3 phase (Price *et al.*, 1999; Reddy and Kumar, 2016), which is consistent with the XPS analysis. With the increase of Se concentration, the vibration peaks become broader and show an obvious red-shift compared with those of the SnS sample.

To determine the band gaps of the Se-doped SnS nanobelts, the diffuse reflectance spectra were recorded. Using Kubelka–Munk function transformation (Herron *et al.*, 2014) and Tauc function (Cho and Sung, 2013), the optical band gaps for the $SnS_{1-x}Se_x$ nanobelts ($x = 0$, 0.097, 0.13, and 0.23) are obtained and found to gradually decrease from 1.15 to 1.01 eV with the increase of Se doping as shown in Figure 5, confirming that the band gaps of the SnS nanobelts have been tuned by Se doping (Wei *et al.*, 2011). Compared to the reported band gap of bulk thermoelectric SnS (between 1.21 and 1.18 eV) (Tan *et al.*, 2014), smaller band gaps are observed for the $SnS_{1-x}Se_x$ nanobelts prepared in this work, which should be due to the Se doping.

IV. CONCLUSION

In conclusion, Se-doped SnS ($SnS_{1-x}Se_x$) nanobelts have been successfully synthesized by a facile hydrothermal method. The $SnS_{1-x}Se_x$ nanobelts are well-crystalized single crystals with a uniform 1D structure. Se elements are doped into the lattice substituting for S, resulting that the optical band gap of $SnS_{1-x}Se_x$ nanobelts decreases from 1.15 to 1.01 eV. The high-quality $SnS_{1-x}Se_x$ single-crystalline nanobelts are promising for near-infrared photodetection due to their tunable band gaps.

ACKNOWLEDGEMENTS

This work was financially supported by the National Natural Science Foundation of China (51672051 and 51702058) and Science and Technology Program of Guangzhou, China (201707010251).

https://doi.org/10.1017/S0885715620000615 Published online by Cambridge University Press

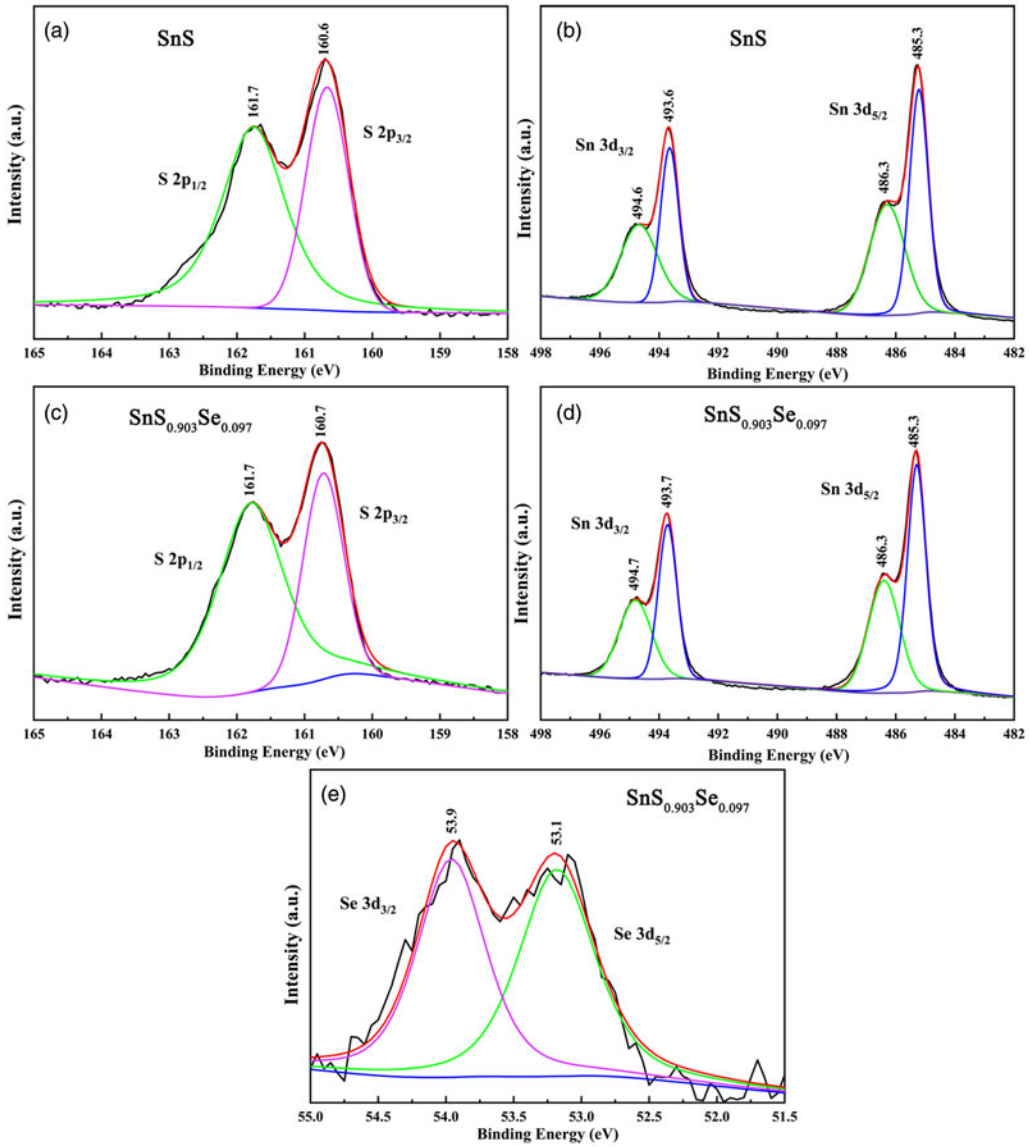

Figure 3. (a) S 2*p* and (b) Sn 3*d* of SnS nanobelts XPS spectra. (c) S 2*p*, (d) Sn 3*d*, and (e) Se 3*d* of $SnS_{0.903}Se_{0.097}$ nanobelts XPS spectra.

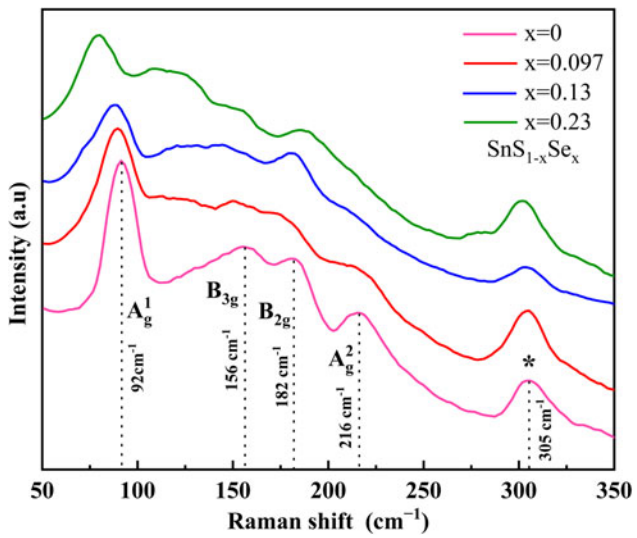

Figure 4. Raman spectra of $SnS_{1-x}Se_x$ nanobelts ($x = 0$, 0.097, 0.13, and 0.23).

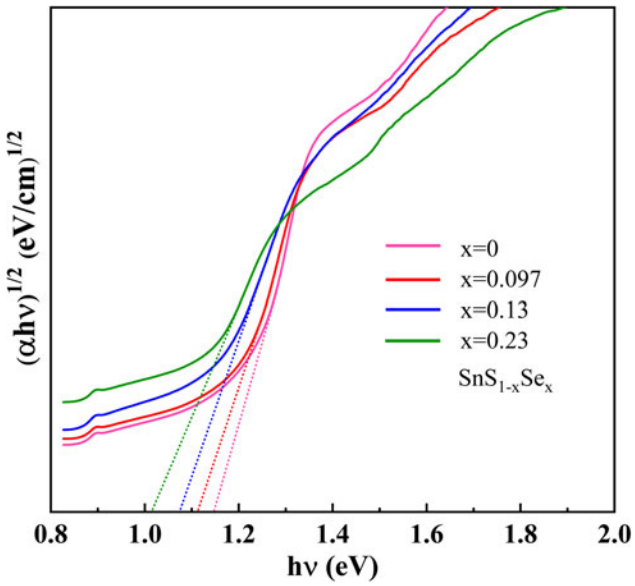

Figure 5. Tauc plot of $SnS_{1-x}Se_x$ nanobelts ($x = 0$, 0.097, 0.13, and 0.23).

https://doi.org/10.1017/S0885715620000615 Published online by Cambridge University Press

Baby, B. H. and Mohan, D. B. (**2019**). "The effect of in-situ and post deposition annealing towards the structural optimization studies of RF sputtered SnS and Sn_2S_3 thin films for solar cell application," Sol Energy **189**, 207–218.

Biçer, M. and Şişman, İ. (**2011**). "Electrodeposition and growth mechanism of SnSe thin films," Appl. Surf. Sci. **257**, 2944–2949.

Biswas, K., He, J. Q., Blum, I. D., Wu, C. I., Hogan, T. P., Seidman, D. N., Dravid, V. P., and Kanatzidis, M. G. (**2012**). "High-performance bulk thermoelectrics with all-scale hierarchical architectures," Nature **489**, 414–418.

Butt, F. K., Cao, C. B., Khan, W. S., Ali, Z., Ahmed, R., Idrees, F., Aslam, I., Tanveer, M., Li, J. L., Zaman, S., and Mahmood, T. (**2012**). "Synthesis of highly pure single crystalline SnSe nanostructures by thermal evaporation and condensation route," Mater. Chem. Phys. **137**, 565–570.

Cao, M., Yao, K. F., Guan, Y. S., Shi, H. Z., Yang, W. G., Huang, J., Sun, Y., Hao, J. M., Wang, L. J., Shen, Y., and Dai, N. (**2019**). "Template-free electrodeposition of SnS nanotubes and their photoelectrochemical properties," Mater. Lett. **250**, 186–188.

Chen, X. L., Cao, Y. G., Lan, Y. C., Xu, X. P., Li, J. Q., Lu, K. Q., Jiang, P. Z., Xu, T., Bai, Z. G., Yu, Y. D., and Liang, J. K. (**2000**). "Synthesis and structure of nanocrystal-assembled bulk GaN," J. Cryst. Growth **209**, 208–212.

Cheng, S. Y. and Conibeer, G. (**2011**). "Physical properties of very thin SnS films deposited by thermal evaporation," Thin Solid Films **520**, 837–841.

Cho, K. H. and Sung, Y. M. (**2013**). "Self-catalytic solution–liquid–liquid–solid (SLLS) growth of tapered SnS nanorods," Nanoscale **5**, 3690–3697.

Franzman, M. A., Thompson, M. E., and Brutchey, R. L. (**2010**). "Solution-phase synthesis of SnSe nanocrystals for use in solar cells," J. Am. Chem. Soc. **132**, 4060–4406.

Guo, J., Jian, J. K., Liu, J., Cao, B. L., Lei, R. B., Zhang, Z. H., Song, B., and Zhao, H. Z. (**2017**). "Synthesis of SnSe nanobelts and the enhanced thermoelectric performance in its hot-pressed bulk composite," Nano Energy **38**, 569–575.

He, W. K., Wang, D. Y., Wu, H. J., Xiao, Y., Zhang, Y., He, D. S., Feng, Y., Hao, Y. J., Dong, J. F., Chetty, R., Hao, L. J., Chen, D. F., Qin, J. F., Yang, Q., Li, X., Song, J. M., Zhu, Y. C., Xu, W., Niu, C. L., Li, X., Wang, G. T., Liu, C., Ohta, M., Pennycook, S. J., He, J. Q., Li, J. F., and Zhao, L. D. (**2019**). "High thermoelectric performance in low-cost $SnS_{0.91}Se_{0.09}$ crystals," Science **365**, 1418–1424.

Herron, S. M., Tanskanen, J. T., Roelofs, K. E., and Bent, S. F. (**2014**). "Highly textured Tin(II) sulfide thin films formed from sheetlike nanocrystal inks," Chem. Mater. **26**, 7106–7113.

Iqbal, M. Z., Wang, F. P., Rafique, M. Y., Ali, S., Farooq, M. H., and Ellahi, M. (**2013**). "Hydrothermal synthesis, characterization and hydrogen storage of SnS nanorods," Mater. Lett. **106**, 33–36.

Kafashan, H., Azizieh, M., and Balak, Z. (**2017**). "Electrochemical synthesis of nanostructured Se-doped SnS: effect of Se-dopant on surface characterizations," Appl. Surf. Sci. **410**, 186–195.

Khan, M. D., Aamir, M., Murtaza, G., Malik, M. A., and Revaprasadu, N. (**2018**). "Structural investigations of $SnS_{1-x}Se_x$ solid solution synthesized from chalcogeno-carboxylate complexes of organo-tin by colloidal and solvent-less routes," Dalton Trans. **47**, 10025–10034.

Li, L. D., Lou, Z., and Shen, G. Z. (**2017a**). "Flexible broadband image sensors with SnS quantum dots/Zn_2SnO_4 nanowires hybrid nanostructures," Adv. Funct. Mater. **28**, 1705389.

Li, W., Zheng, L. L., Ge, B. H., Lin, S. Q., Zhang, X. Y., Chen, Z. W., Chang, Y. J., and Pei, Y. Z. (**2017b**). "Promoting SnTe as an eco-friendly solution for p-PbTe thermoelectric via band convergence and interstitial defects," Adv Mater. **29**, 1605887.

Liu, J., Jian, J. K., Yu, Z. Q., Zhang, Z. H., Cao, B. L., and Du, B. S. (**2017**). "Catalyst-free vapor phase growth of ultralong SnSe single-crystalline nanowires," Cryst. Growth Des. **17**, 6163–6168.

Lu, J., Nan, C. Y., Li, L. H., Peng, Q., and Li, Y. D. (**2012**). "Flexible SnS nanobelts: facile synthesis, formation mechanism and application in Li-ion batteries," Nano Res. **6**, 55–64.

Lu, C. L., Zhang, Y. W., Zhang, L., and Yin, Q. (**2019**). "C/SnS bilayer structures fabricated via electrodeposition," Appl. Surf. Sci. **484**, 560–567.

Price, L. S., Parkin, I. P., Hardy, A. M. E., and Clark, R. J. H. (**1999**). "Atmospheric pressure chemical vapor deposition of tin sulfides (SnS, Sn_2S_3, and SnS_2) on glass," Chem. Mater. **11**, 1792–1799.

Ramakrishna Reddy, K. T., Koteswara Reddy, N., and Miles, R. W. (**2006**). "Photovoltaic properties of SnS based solar cells," Sol. Energ. Mat. Sol. C **90**, 3041–3046.

Reddy, T. S. and Kumar, M. C. S. (**2016**). "Effect of substrate temperature on the physical properties of co-evaporated Sn_2S_3 thin films," Ceram. Int. **42**, 12262–12269.

Sarkar, A. S., Mushtaq, A., Kushavah, D., and Pal, S. K. (**2020**). "Liquid exfoliation of electronic grade ultrathin tin(II) sulfide (SnS) with intriguing optical response," Npj 2D Mater. Appl. **4**, 1–9.

Sohila, S., Rajalakshmi, M., Ghosh, C., Arora, A. K., and Muthamizhchelvan, C. (**2011**). "Optical and Raman scattering studies on SnS nanoparticles," J. Alloys Compd. **509**, 5843–5847.

Steichen, M., Djemour, R., Gütay, L., Guillot, J., Siebentritt, S., and Dale, P. J. (**2013**). "Direct synthesis of single-phase p-type SnS by electrodeposition from a dicyanamide ionic liquid at high temperature for thin film solar cells," J. Phys. Chem. C **117**, 4383–4393.

Suryawanshi, S. R., Warule, S. S., Patil, S. S., Patil, K. R., and More, M. A. (**2014**). "Vapor-liquid-solid growth of one-dimensional tin sulfide (SnS) nanostructures with promising field emission behavior," ACS Appl. Mater. Interfaces **6**, 2018–2025.

Tan, Q., Zhao, L. D., Li, J. F., Wu, C. F., Wei, T. R., Xing, Z. B., and Kanatzidis, M. G. (**2014**). "Thermoelectrics with earth abundant elements: low thermal conductivity and high thermopower in doped SnS," J. Mater. Chem. A **2**, 17302–17306.

Vidal, J., Lany, S., d'Avezac, M., Zunger, A., Zakutayev, A., Francis, J., and Tate, J. (**2012**). "Band-structure, optical properties, and defect physics of the photovoltaic semiconductor SnS," Appl. Phys. Lett. **100**, 032104.

Wang, Q. S., Yao Wen, Y., Yao, F. R., Huang, Y., Wang, Z. X., Li, M. L., Zhan, X. Y., Xu, K., Wang, F. M., Wang, F., Li, J., Liu, K. H., Jiang, C., Liu, F. Q., and He, J. (**2015**). "BN-enabled epitaxy of $Pb_{1-x}Sn_xSe$ nanoplates on SiO_2/Si for high-performance mid-infrared detection," Small **11**, 5388–5394.

Wei, H., Su, Y. J., Chen, S. Z., Lin, Y., Yang, Z., Chen, X. S., and Zhang, Y. F. (**2011**). "Novel SnS_xSe_{1-x} nanocrystals with tunable band gap: experimental and first-principles calculations," J. Mater. Chem. **21**, 12605–12608.

Yao, J. D., Zheng, Z. Q., and Yang, G. W. (**2017**). "All-layered 2D optoelectronics: a high-performance UV-Vis-NIR broadband SnSe photodetector with Bi_2Te_3 topological insulator electrodes," Adv. Funct. Mater. **27**, 1701823.

Yue, G. H., Lin, Y. D., Wen, X., Wang, L. S., Chen, Y. Z., and Peng, D. L. (**2011**). "Synthesis and characterization of the SnS nanowires via chemical vapor deposition," Appl. Phys. A **106**, 87–91.

Zhang, J. B., Gao, J. B., Church, C. P., Miller, E. M., Luther, J. M., Klimov, V. I., and Beard, M. C. (**2014**). "PbSe quantum dot solar cells with more than 6% efficiency fabricated in ambient atmosphere," Nano Lett. **14**, 6010–6015.

Zhao, N., Osedach, T. P., Chang, L. Y., Geyer, S. M., Wanger, D., Binda, M. T., Arango, A. C., Bawendi, M. G., and Bulovic, V. (**2010**). "Colloidal PbS quantum dot solar cells with high fill factor," ACS Nano **4**, 3743–3752.

Zhao, L. D., Lo, S. H., Zhang, Y. S., Sun, H., Tan, G. J., Uher, C., Wolverton, C., Dravid, V. P., and Kanatzidis, M. G. (**2014**). "Ultralow thermal conductivity and high thermoelectric figure of merit in SnSe crystals," Nature **508**, 373–377.

Zhou, X., Gan, L., Zhang, Q., Xiong, X., Li, H. Q., Zhong, Z. Q., Han, J. B., and Zhai, T. Y. (**2016**). "High performance near-infrared photodetectors based on ultrathin SnS nanobelts grown via physical vapor deposition," J. Mater. Chem. C **4**, 2111–2116.